

A Multisensory Edge-Cloud Platform for Opportunistic Radio Sensing in Cobot Environments

Sanaz Kianoush, *member, IEEE*, Stefano Savazzi, *member, IEEE*, Manuel Beschi, Stephan Sigg, *member, IEEE*, and Vittorio Rampa, *member, IEEE*

Abstract—Worker monitoring and protection in collaborative robot (cobots) industrial environments requires advanced sensing capabilities and flexible solutions to monitor the movements of the operator in close proximity of moving robots. Collaborative robotics is an active research area where Internet of Things (IoT) and novel sensing technologies are expected to play a critical role. Considering that no single technology can currently solve the problem of continuous worker monitoring, the paper targets the development of an IoT multisensor data fusion (MDF) platform. It is based on an edge-cloud architecture that supports the combination and transformation of multiple sensing technologies to enable the passive and anonymous detection of workers. Multidimensional data acquisition from different IoT sources, signal pre-processing, feature extraction, data distribution and fusion, along with machine learning (ML) and computing methods are described. The proposed IoT platform also comprises a practical solution for data fusion and analytics. It is able to perform opportunistic and real-time perception of workers by fusing and analyzing radio signals obtained from several interconnected IoT components, namely a multi-antenna WiFi installation (2.4-5 GHz), a sub-THz imaging camera (100 GHz), a network of radars (122 GHz) and infrared sensors (8-13 μm). The performance of the proposed IoT platform is validated through real use case scenarios inside a pilot industrial plant in which protective human-robot distance must be guaranteed considering latency and detection uncertainties.

Index Terms—Multisensor data fusion, passive radio sensing, transformative computing, cloud-assisted Internet of Things, real-time data analysis, robot assisted manufacturing.

I. INTRODUCTION

NEXT generation manufacturing, namely Industry 4.0 (I4.0), must ensure workspace safety and production efficiency during human-robot cooperation (HRC). Within this context, human safety must be guaranteed by continuously and accurately sensing and tracking worker activities. Perception of workers in highly dynamic environments thus becomes the key to achieve a high level of efficiency and flexibility that is required by the foreseen I4.0 applications [1], [2]. Dynamic collaborative robot (cobot) environments entail reconfigurable layouts, high degrees of shared resources, and humans moving

S. Kianoush, S. Savazzi and V. Rampa are with the Institute of Electronics, Computer and Telecommunication Engineering (IEIT) of Consiglio Nazionale delle Ricerche (CNR), p.zza Leonardo da Vinci, 20133 Milano, Italy, e-mail: {sanaz.kianoush, stefano.savazzi, vittorio.rampa}@ieit.cnr.it.

M. Beschi is with the Institute of Sistemi e Tecnologie Industriali Intelligenti per il Manifatturiero Avanzato (STIIMA), of Consiglio Nazionale delle Ricerche (CNR), Milano, Italy, e-mail: {manuel.beschi@stiima.cnr.it.

Stephan Sigg is with Aalto University, Department of Communications and Networking, Finland, e-mail: {stephan.sigg}@aalto.fi.

This work has been partially funded by MUR Italy and Academy of Finland within the ERA-NET CO-FUND H2020 CHISTERA III project RadioSense.

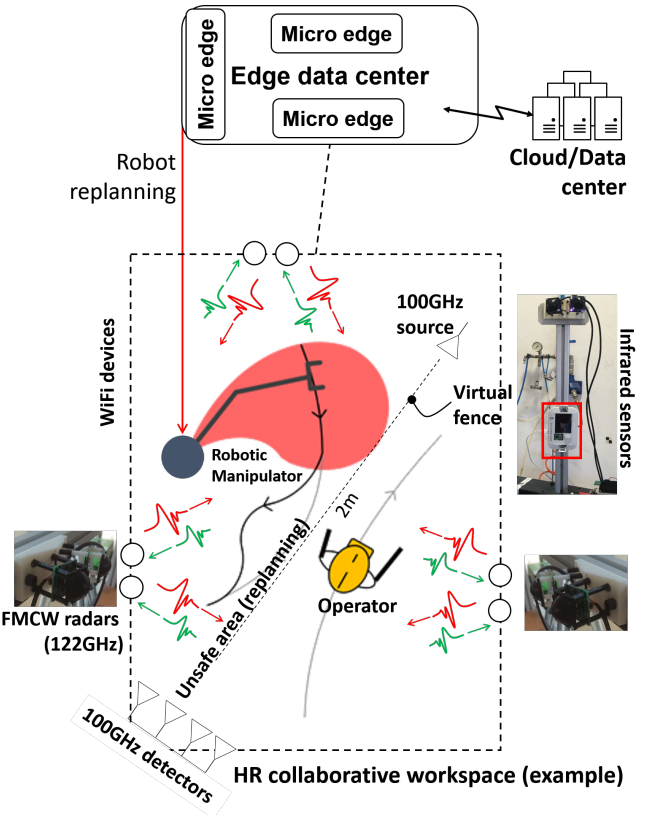


Fig. 1. Multisensory platform and collaborative HR workspace consisting of a robotic manipulator and a worker in a fenceless shared space.

in loosely structured, fenceless workplaces [3] interacting with multiple machines [4]. Collaborative robotics is a fairly unique and challenging application where Internet of Things (IoT) technologies are expected to play a pivotal role. In this context, the reuse, or transformation [5], of sensors [6] and their orchestration through reliable and low-latency machine-type communications [7] (5G wireless technologies [8]) represent the principal components for more integrated, adaptive, configurable and, above all, safer manufacturing environment.

Recently, techniques to capture and process the wireless stray electromagnetic (EM) radiations originated from different radio sources are gaining increasing attention [9], [10]. In particular, these techniques can be exploited for privacy-preserving human-scale sensing [11], human behavior recognition, detection/localization, as well as crowd density estimation and mapping. For example, passive RF sensing, or radio

vision [10], leverages different radio frequency (RF) technologies for sensing tasks. RF signals are perturbed by moving objects/bodies, and by changing configurations, due to the propagation of transmitted, reflected, scattered and diffracted EM waves. Hence, in addition to transporting modulated information, they can serve as virtual sensors to infer two- or three-dimensional (2D/3D) views of all objects traversed by the EM wavefield.

Previous work on sensing for HRC usually focused the design of individual technologies, such as wearables [2], vision [6], radars [12], or machine type communications [13]. However, it is expected that the combination and transformation of multiple sensing technologies will be the key to meet the expected localization accuracy in cobot environments [6]. The paper proposes the integration of heterogeneous RF sensing technologies into an industry-compliant IoT-based edge-cloud computing architecture to provide augmented information about worker safety in the context of HRC manufacturing. Fig. 1 shows a schematic of the proposed IoT Multisensor Data Fusion (MDF) platform inside a robotic cell consisting of an industrial manipulator and a human worker, along with an edge-cloud computing architecture for data distribution and processing. The robotic cell implements the closed-loop control of the manipulator activities to guarantee worker safety. This control loop is underpinned by the proposed human sensing tool: accuracy and latency tradeoff is analyzed to achieve safety monitoring of the workspace, namely to minimize the human-robot protective distance.

II. LITERATURE REVIEW AND CONTRIBUTIONS

Opportunistic sensing targets the cross-fertilization of computing and communication technologies, leveraging opportunistically different ambient signals (*e.g.*, radio, acoustic, light). The compound effect of heterogeneous sensors is expected to improve accuracy and to enable new capabilities. Technologies for opportunistic and transformative radio sensing, such as device-free radio localization, activity recognition [14], and people counting [15], typically focus on the augmentation and transformation of existing radio devices, such as WiFi, machine-type communication (MTC) or cellular-wireless wide area networks (WWAN) [16] into human-scale sensors. These radio technologies generally exploit electromagnetic (EM) fields maintained by different sources (*i.e.*, infrared, micro-wave and 100–122 GHz, bands). Measurements of such EM fields are used to extract an image of the environment, or its modifications, for various motion perception tasks [12]. In particular, the human presence in the environment changes the EM propagation characteristics due to reflection, scattering and diffraction. In [15], WiFi signals are used for target counting and activity recognition while, in [17], a cloud-IoT platform is proposed to sustain device-free human sensing by real time processing of the channel quality information (CQI). In order to manage high-dimensional data processing and real-time analysis, a cloud platform along with machine learning tools are proposed. Multidimensional data analytics is therein implemented by exploiting WiFi signals, while the problems related to data

fusion, edge-side computations and service orchestration are not discussed. In [20], a device-free localization and fall detection system has been proposed for HRC applications. It adopts unmodified machine type radio communications based on the IEEE 802.15.4 standard.

All above mentioned works focus on the evaluation of individual technologies for human sensing; however, they also demonstrate that no single sensing technology can provide robust and accurate sensing information.

A. Human-Robot Cooperation and Sensors

In recent years, industrial robotic cells have been subjected to a paradigm shift, where physical fences have been removed to save space and to increase the interaction between workers and robots [21]. HRC is a key enabler in advanced manufacturing, allowing the human workers to be assisted by cobots for collaborative execution of complex repetitive workflows. Effectiveness in HRC tasks largely depends on the possibility to allow a human operator a great autonomy in decision making, task execution order and timing. Examples include, but are not limited to holding/resuming some tasks, temporarily leaving workstations for contingencies, buffering and re-sequencing production steps [22].

Advanced HRC tasks involving worker co-presence will be underpinned by IoT technologies supporting new human-scale monitoring and perception tools. Focusing on human sensing in the context of cobot environments, the standard ISO/TS 15066 [25] describes the specifications of the speed and separation monitoring (SSM) collaborative operations. SSM allows robots and workers to share the same workspace while the robot has to reduce its speed or/and to follow an alternative path according to the worker's position. An effective implementation of SSM requires the online detection of the relative distance d between the robot and the worker. This distance is time-sensitive and must be compared in real-time with the *protective separation distance* d_p , namely the minimum permissible human-robot distance. In turn, the protective distance depends on the uncertainties of the positions of both robot and human, as well as the relative velocity between the worker and the robot, and the latencies of the system. The protective distance d_p must be minimized to guarantee an efficient collaborative space. In addition, the constraint $d > d_p$ must be verified during all collaborative activities. As analyzed in detail in Sect. VI, the protective distance d_p depends on the reaction time, latency and positioning uncertainties that should be quantified according to the deployed sensing system.

In what follows, we refer to localization in terms of *anonymous* (*i.e.*, passive, or device-free) detection of motion and location, as opposed to *active* tracking where identity tagging occurs [2]. Localization services enabled by the proposed IoT MDF platform should be able to map increasingly complex figures such as:

- *pose*, namely application-space current location coordinates of workers (and cobots);
- *trajectory*: first/second order kinematics used for tracing the projection of the current pose and predicting space occupancy;

- *behaviors*: full trajectory patterns associated with some specific worker activity and semantics.

Pose and trajectory estimation are here explored in detail as necessary for maintaining the protective distance d_p . Behavior detection is used to anticipate potentially hazardous situations. Considering that the effectiveness of pose and trajectory estimation depends on latency and localization uncertainties, we explore the compound effect of multiple passive radio sensing technologies with the goal of optimizing d_p .

Mainstream safety technologies make use of dedicated sensors to detect presence, tracing displacements or distances. Optoelectronic devices [6] typically exploit the properties of reflectivity, while other technology uses emissivity of thermal images or acoustic fields. The major downsides of these systems are the full-accuracy ranges, the presence of occlusions, the environmental conditions (*e.g.*, dust, fumes) and, for those based on vision tracking, privacy concerns. Orchestration of these sensors, through collaborative approaches and data fusion systems based on machine learning, is a critical problem and still considered open [31]. Besides cooperation of interconnected sensors, transformative, or opportunistic sensing [5] adapts the individual IoT devices to support advanced tasks, far beyond their original designs.

B. Contributions

The paper targets the design of an ecosystem of heterogeneous IoT radio-based systems that combines and transforms multiple RF sources/detectors into different *virtual* sensors. These sensing modalities are all instrumental to workspace monitoring and enable three key *HRC functions*: *i*) the identification of the number of workers present in the workspace, *ii*) the localization of the worker inside the operating space ($d > 1$ m) and *iii*) the monitoring of the HR distance inside the collaborative space ($d < 1$ m). As depicted in Fig. 1, different passive radio sensing IoT devices cooperate to achieve opportunistic and anonymous perception of the worker when sharing the space with a robot. In particular, the proposed MDF platform combines IoT sensors that detect infrared (IR) body emissions in the short-range, multi-antenna WiFi radios that monitor body-induced reflections, a network of radars monitoring the sub-THz (122 GHz) band, and a sub-THz imaging source/camera (100 GHz). Cooperation and coordination of heterogeneous sensors is based on a cloud-edge platform. Considering that multiple radios and sensing sources are employed, we also propose a practical feature-based solution for data fusion and analytics. Features, namely uniform statistical representations of raw data from different sensors, are obtained by edge units. These units are responsible for pre-processing and data fusion. Analytics is carried out in the cloud and it is based on the processing of the features published by the edge units. The proposed cloud-edge MDF platform is designed to process large amounts of (multi-dimensional) raw data [17] and adopts different machine learning (ML) tools that expect individual, or combinations of, features as input, depending on the HRC function.

The paper is organized as follows: the cloud-edge MDF platform is introduced in Sect. III, considering feature extraction from pre-processed raw data, feature fusion implemented

on a dedicated edge device, analytics on the cloud back-end, and related communication aspects, respectively. In particular, the edge node consists of multiple micro servers/data centers (micro-edges) for extracting, processing and fusing features from different sensors (pipelines). Focusing on an HRC workspace scenario where the edge node is configured to monitor an individual robotic cell (Fig. 1), the IoT components, sensors and data pre-processing tools are discussed in Sect. IV. Extensive experimental activities inside the robotic cell have been conducted in Sect. V to assess the feasibility and performance of the platform considering the three HRC functions previously mentioned. The goal is to find the best performance trade-off in terms of fused data/features volume (*i.e.*, number of sensors and data size), accuracy and latency for real-time implementation. Based on such analysis, in Sect. VI we evaluate the robustness of the system in terms of the protective human–robot separation distance d_p . Protective distance is underpinned by accuracy and latency, that are both quantified for the selected HRC functions. Concluding remarks and open problems are highlighted in Sect. VII.

III. MULTISENSOR DATA FUSION PLATFORM: FEATURE EXTRACTION, FUSION AND ANALYTICS

MDF platforms [18] provide accurate, reliable and timely measurements of a physical process by combining sensor data. Sensors provide measurement data to the sensor fusion level where a fusion algorithm is used to extract and process information. MDF system architectures can be centralized, de-centralized, distributed or hierarchical [19]. The platform adopted here is depicted in Fig. 2: it consists of distributed edge units each assigned to monitor an individual workspace area around a robot (*i.e.*, the robotic cell) and a cloud server in charge of analytics tasks. The edge unit organizes the processing of data obtained from the corresponding sensors into N *data processing pipelines*, each managed by a dedicated server (*micro-edge*). Each data processing pipeline consists of a group of M sensors whose raw data require similar pre-processing stages, including data abstraction from raw radio signals and de-noising (*i.e.*, background subtraction). Considering M sensors and N pipelines, the raw data $\mathbf{X}_{k,i}(t)$ at time t obtained from sensor $k = 1, \dots, M$ and pipeline $i = 1, \dots, N$ follows sensor-specific pre-processing stages represented by the operator $f_i(\cdot|\phi_i)$

$$\tilde{\mathbf{X}}_{k,i}(t) = f_i(\mathbf{X}_{k,i}|\phi_i) \quad (1)$$

that uses pipeline-dependent parameters ϕ_i . Pre-processing is described in Sect. IV based on the chosen devices and sensing hardware. The edge units are in charge of extracting *features* using the de-noised $\tilde{\mathbf{X}}_{k,i}(t)$ time series as inputs. The features, described in Sect. III-A, are statistical, low dimensional, representations of $\tilde{\mathbf{X}}_{k,i}(t)$. Features have a uniform representations across different pipelines. Therefore, they can be easily combined, or fused, and jointly analyzed. The selection of features to be fused depends on the implemented HRC function and it is managed by the cloud server, through the data controller. Machine learning (ML) tools for analytics on input features (classification) are described in Sect. III-B.

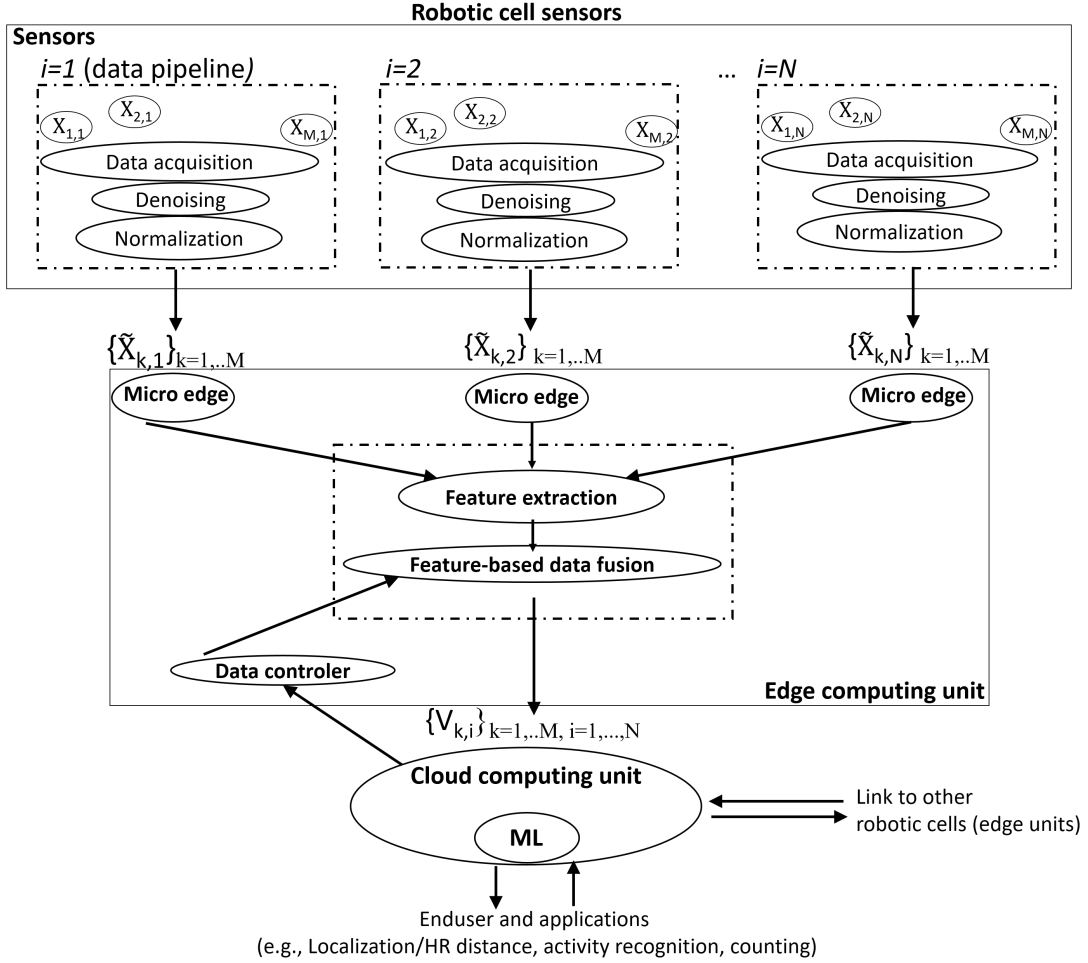


Fig. 2. Multisensor data fusion system model and data analytics

A. Edge node: data distribution, feature extraction and fusion

We focus here on data distribution at the edge of the MDF platform, and from the edge to the cloud unit as well. As shown in Fig. 3, the edge node contains N micro-edges. They act as dedicated servers/brokers for the corresponding data pipeline carrying de-noised data $\tilde{\mathbf{X}}_{k,i}(t)$. Considering telemetry collection on each pipeline, both the de-noised data $\tilde{\mathbf{X}}_{k,i}(t)$ and the corresponding time-stamp (t) information are represented by JavaScript Object Notation (JSON) structures. Sensor data $\tilde{\mathbf{X}}_{k,i}(t)$ is sent by the individual sensors through a wireless network supporting both WiFi and IEEE 802.15.4 2.4 GHz standards (see Sect. V for further details). For transport level, both RESTful Web Services and Message Queuing Telemetry Transport (MQTT) can be adopted inside each micro-edge. Therefore, when using HTTP transport (RESTful) the micro-edge acts as a dedicated server exposing resources. On the contrary, during MQTT transport, it acts as broker, accepting subscriptions from the specific pipeline for telemetry publishing. Finally, the micro-edges also provide computing, storage and caching functions [47] for the corresponding pipeline.

Each i -th micro-edge is in charge of mid-level data analytics for the corresponding pipeline. It processes the corresponding

de-noised data-sets $\{\tilde{\mathbf{X}}_{1,i}(t), \dots, \tilde{\mathbf{X}}_{M,i}(t)\}$ to obtain the high level *features* $\mathbf{V}_i = \{V_{1,i}, \dots, V_{M,i}\}$ for the considered pipeline. Features are obtained individually at the edge node; however, the cloud unit can supervise such stage through a data controller feedback (Fig. 3) that is used to select the features to be processed based on the specific HRC function as shown in Sect. V. In particular, considering the data $\tilde{\mathbf{X}}_{k,i}(t)$ from pipeline i and sensor k , four distinctive statistical representations $V_{k,i} = \{\mu_{k,i}, \sigma_{k,i}, \zeta_{k,i}, \kappa_{k,i}\}$ are used as features where

$$\begin{aligned}
 \mu_{k,i} &= \mathbb{E}_t [\tilde{\mathbf{X}}_{k,i}(t)] \\
 \sigma_{k,i} &= \sqrt{\mathbb{E}_t \left[\left(\tilde{\mathbf{X}}_{k,i}(t) - \mu_{k,i} \right)^2 \right]} \\
 \zeta_{k,i} &= \mathbb{E}_t \left[\left(\frac{\tilde{\mathbf{X}}_{k,i}(t) - \mu_{k,i}}{\sigma_{k,i}} \right)^3 \right] \\
 \kappa_{k,i} &= \mathbb{E}_t \left[\left(\frac{\tilde{\mathbf{X}}_{k,i}(t) - \mu_{k,i}}{\sigma_{k,i}} \right)^4 \right].
 \end{aligned} \tag{2}$$

$\mu_{k,i}$ and $\sigma_{k,i}$ are the mean and the standard deviation, while $\zeta_{k,i}$ and $\kappa_{k,i}$ track the skewness (*i.e.*, third moment) and the kurtosis (*i.e.*, fourth moment) coefficients evaluated over consecutive time samples. As shown in Fig. 3, output features are again serialized by the edge node using JSON

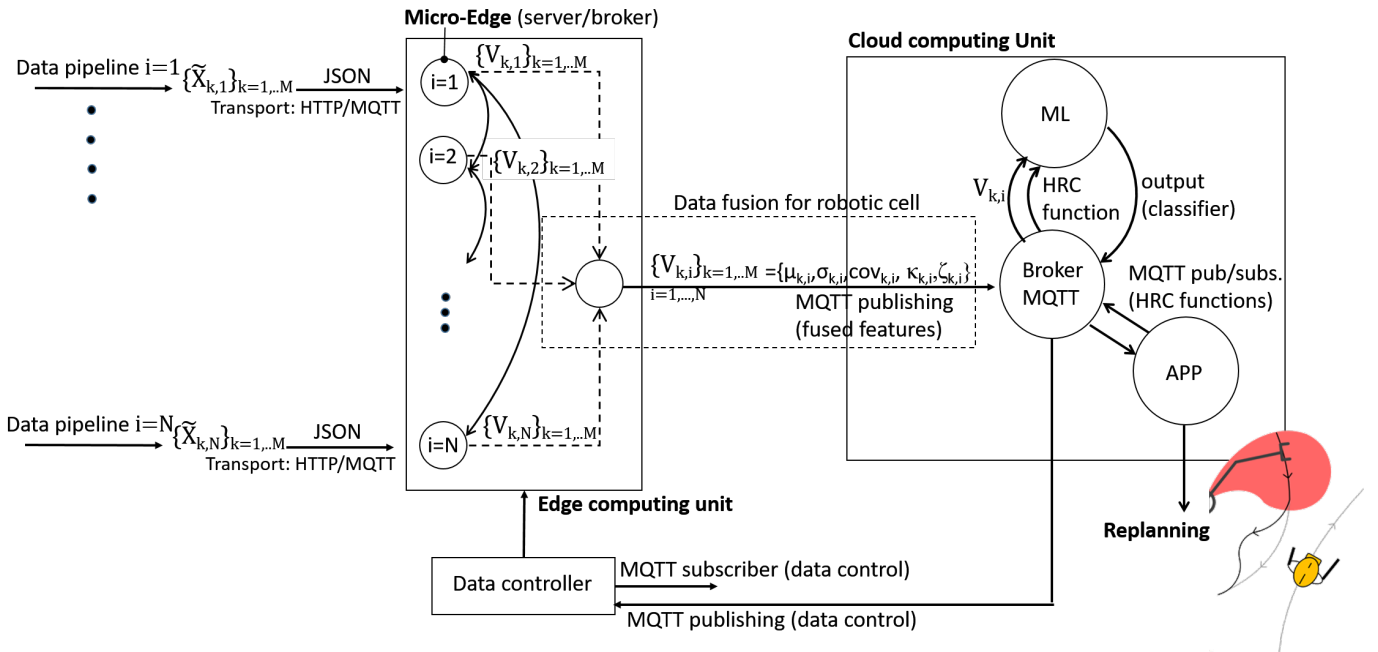


Fig. 3. Software architecture of the edge/cloud MDF platform: feature computing, data fusion, distribution and transport layers.

representation and sent to the cloud using MQTT as transport layer.

B. Cloud unit: feature analytic tools and HRC functions

The cloud unit processes the features (2) published by the edges to infer a hidden process. Considering the three HRC functions introduced in Sect. II-B, the corresponding hidden processes are: *i*) the number of subjects in the workspace (worker counting); *ii*) their positions inside the operating space (occupancy), and *iii*) the human-robot distance d (co-presence monitoring). The cloud uses a ML model to process a selected subset of features. The ML model and the feature subset are optimized using a supervised approach that is based on training data collected inside the HRC environment. In particular, the Long-Short Term Memory (LSTM) and the Convolutional Neural Network (CNN) models are chosen for real-time manipulation of heterogeneous feature streams. Opportunities and limitations of both models are considered in Sect. V.

With respect to end-user interfacing, third party applications can subscribe to the cloud, via MQTT messaging, for a specific HRC function of interest, and wait for real-time results pushed back by the ML unit, through the cloud service broker. The cloud unit thus provides an open layer between end-user applications and the underlying feature manipulation resources.

IV. OPPORTUNISTIC RADIO SENSING INSIDE THE COLLABORATIVE SPACE

The robotic cell, depicted in Fig. 4, consists of one manipulator performing a pick and place activity in proximity of an assembly line. The MDF platform adopts $N = 4$ pipelines and a wide range of IoT passive radio sensing devices operating

in the sub-THz (100 – 122 GHz), microwave (2.4 – 5 GHz), and long-wavelength infrared (LWIR) (8 – 13 μm) bands from which it is possible to infer the EM radiation as perturbed by the presence of the worker and the robot, or the thermal IR radiation as emitted by the human subject being measured, respectively. In this section, we describe the IoT sensors deployed, the signal model and the data pre-processing stages (equation 1) implemented by the individual pipelines.

A. Sub-THz radars and detectors

The sub-THz radiation refers to the frequency band between 0.1 THz and 1 THz. In this band, the propagation is extremely sensitive to environmental changes and presence of chemical/biological agents [33] typically affect both EM spreading and absorption losses. Beside sensing, THz band communication [34] is also expected to be widely applied in industrial applications [35]. Compared to passive sensing technologies in the microwave 1 – 50 GHz band, the adoption of sub-THz signals is expected to provide precise imaging in the short range, as well as reduced multipath effects, to further increase the accuracy of human-scale sensing in exchange of a more limited coverage area. The MDF platform combines two sub-THz sensor systems managed by two distinct pipelines: *i*) a network of Frequency Modulated Continuous Wave (FMCW) radars working at 122 GHz [36] that are deployed for the passive localization of workers in the robotic cell, and *ii*) a 2D array of co-located THz detectors [12] monitoring the intensity of the radiation emitted by a sub-THz generator (100 GHz) in the surroundings of the robot.

FMCW radars are deployed along the perimeter of the robotic cell and process the received beat signals corresponding to echoes from a target/obstacle that are mixed with the transmitted signal. The transmitted signal is a sweep frequency modulated (FM) continuous wave (CW) with bandwidth up

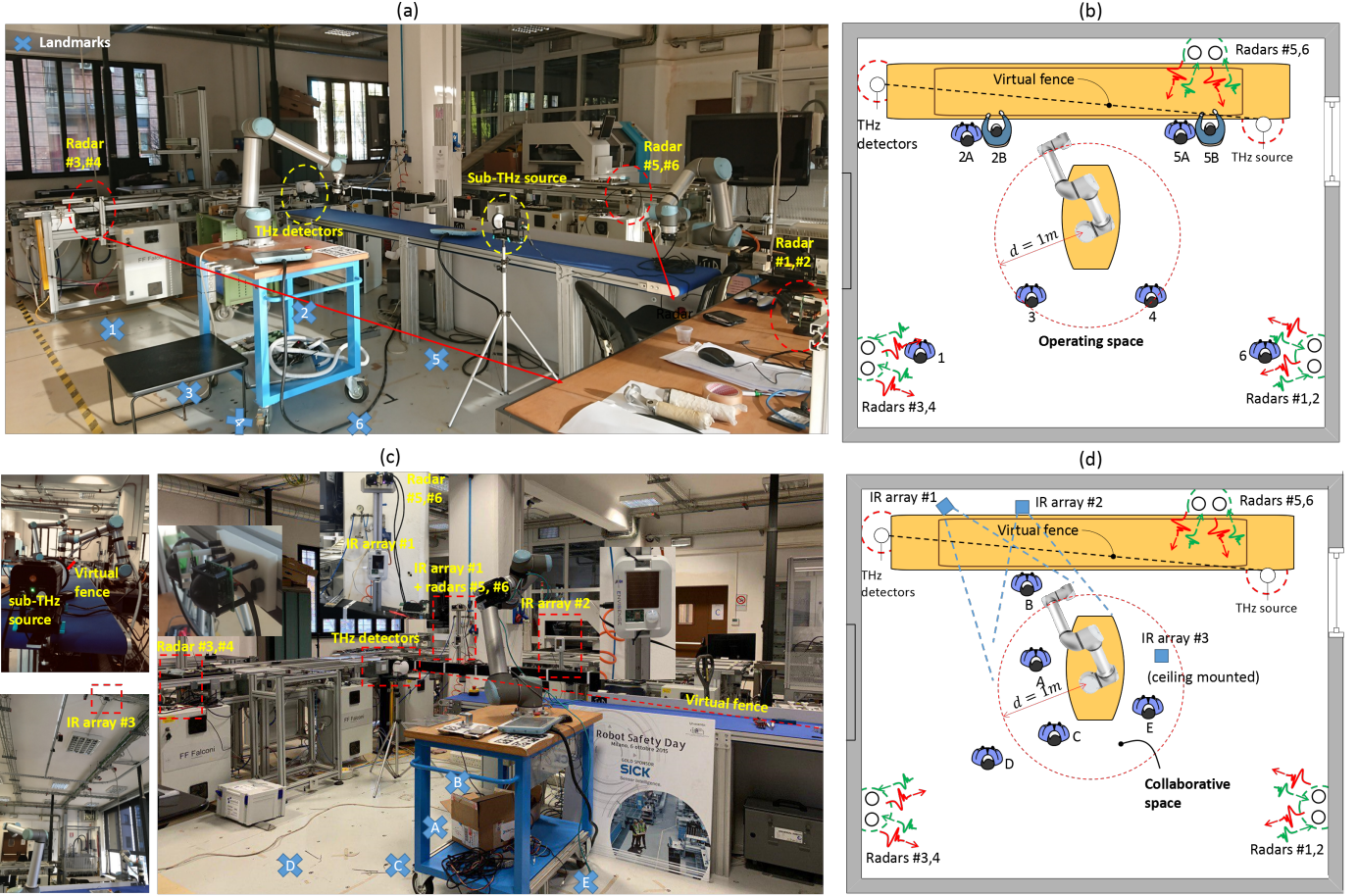


Fig. 4. Industrial pilot plant, robot, and sensor deployment: a) robotic cell environment with sub-THz radar and detector deployment; b) landmark positions for worker motion detection ($d > 1$ m); c) IR arrays and THz sensors deployment; d) landmark positions for worker-robot co-presence monitoring ($d < 1$ m).

to 6 GHz and ramp (pulse) duration of $T = 1$ ms. The carrier frequency is set in the nominal 122 GHz ISM (Industrial Scientific and Medical) band. Beat signals are first converted in the frequency domain by 512-point Fast Fourier Transform (FFT) and averaged over 8 consecutive frames. Fig. 5 on top shows selected FFT images from $M = 6$ radars versus time, collected in an empty and an occupied robotic cell. FFT images are clearly sensitive to the presence of the worker. Assuming that radars are processed by pipeline $i = 1$, for radar $k \in [1, \dots, M]$ and time t , the corresponding $N_{FFT} = 512$ FFT samples

$$\mathbf{X}_{k,1}(t) = [x_{k,t}(1), \dots, x_{k,t}(N_{FFT})] \quad (3)$$

undergo pre-processing steps, namely $\tilde{\mathbf{X}}_{k,1}(t) = f_1(\mathbf{X}_{k,1} | \phi_1 = [\mathbf{C}_k, \bar{\mathbf{X}}_k(\theta)])$, for de-noising and background $\bar{\mathbf{X}}_k(\theta)$ subtraction [37] as

$$\tilde{\mathbf{X}}_{k,1}(t) = \mathbf{C}_k^{-\frac{1}{2}} [\mathbf{X}_{k,1}(t) - \bar{\mathbf{X}}_k(\theta)], \quad (4)$$

where $\bar{\mathbf{X}}_k(\theta) = \mathbb{E}_t[\mathbf{X}_{k,1}(t | \theta)]$ is the time average FFT of the beat signal $\mathbf{X}_{k,1}(t | \theta)$ observed in the *empty* robotic cell (θ), namely the background, while \mathbf{C}_k is the covariance matrix $\mathbf{C}_k = \mathbb{E}_t[(\mathbf{X}_{k,1}(t | \theta) - \bar{\mathbf{X}}_k(\theta))(\mathbf{X}_{k,1}(t | \theta) - \bar{\mathbf{X}}_k(\theta))^H]$. Covariance takes into account any environmental change (*i.e.*,

due to concurrent robot movements) that might alter the backscattered wavefield, yet without constituting any alert for worker safety. The de-noised FFT time series $\tilde{\mathbf{X}}_{k,1}(t)$ are processed by the edge unit to track the relative distance of the worker from the robot, from which body movements as well as HR separation distance (d) can be inferred¹. Combining/fusing selected radar output features with other RF sensors enable more advanced worker perception modalities as discussed in Sect. V.

Sub-THz detectors capture the sub-THz radiation originated from a radio source (about 80 mW at carrier frequency 100 GHz) generated by an IMPATT (Impact ionization Avalanche Transit-Time) diode [38]. The M detectors ($M = 1024$) are arranged over a 2D array of (32×32) elements forming a sub-THz camera with rectangular shape. Each sub-THz detector, developed by [39], is sensitive in the $0.05 - 0.7$ THz band with noise-equivalent power of $1 \text{ nW}/\sqrt{\text{Hz}}$. The 2D array captures the presence of the worker moving in the surrounding of the line-of-sight (LOS) path connecting the sub-THz source and the camera. Considering the pipeline $i = 2$, $\mathbf{X}_{k,2}(t)$ is a measure of the $[0 - 1]$

¹we assume the manipulator (robot) position as known, analysis of human and robot position uncertainty is considered in Sect. VI

normalized intensity, or strength, of the radiated sub-THz field observed by the detector $k \in [1, \dots, M]$ of the array at time t . Likewise, for FMCW radars, Fig. 5 shows an example of the normalized signal intensity measured by the 2D array. The measured intensity is proportional to the electric field power of the received electromagnetic waves: any change of the received signal intensity corresponds to different worker body parts obstructing the radio link (*e.g.*, torso, arms and hands). In general, the multi-ray propagation between the fixed sub-THz source and the k -th detector consists of line-of-sight (LOS), reflected, scattered and diffracted rays [12]. When no obstacles are present near the LOS path and the sub-THz setup is directional (*e.g.*, using dielectric lenses as in the experimental setup), the propagation is mostly due to the main LOS ray that depends only on the free-space loss and the absorption loss. Therefore, the radiation intensity is modelled as

$$X_{k,2}(t) = S_k(t) + W_k(\emptyset), \quad (5)$$

where $S_k(t)$ corresponds to the body-induced signature and $W_k(\emptyset) \sim \mathcal{N}(b_k, \sigma_k^2)$ models the background radiation observed in the empty robotic cell. Each background component W_k is modeled here as an independent Gaussian term with average intensity b_k and deviation σ_k^2 . The average component b_k is a function of LOS terms: absorption and free-space loss [12]. Reflection, scattering and diffraction effects due to a worker or the robot near the LOS path introduce time-varying changes of radiation intensity modeled by deviation σ_k^2 . Post-processed data $\tilde{X}_{k,2}(t)$ consists of signatures that are estimated from the input radiation measurements $X_{k,2}(t)$ through subtraction and de-noising, $\tilde{X}_{k,2}(t) = f_2(X_{k,2}|\phi_2 = [b_k, \sigma_k])$,

$$\tilde{X}_{k,2}(t) = \sigma_k^{-1}(X_{k,2}(t) - b_k). \quad (6)$$

In Sect. V, we exploit the sub-THz radio technology to implement a virtual safety fence and monitor the worker presence close by the assembly line.

B. IR array sensors and body-induced thermal signatures

The use of thermal sensors for human body sensing [40] is becoming attractive in many IoT-relevant scenarios, such as smart spaces, assisted living and industrial automation [41]. Thermal vision and related computing tools enable the possibility of analyzing body induced thermal signatures for detection of body motions, fall detection, as well as discriminating those signatures from the environment. The experimental validation scenario of Sect. V exploits $M = 3$ sensors. Each sensor consists of an array of $N_{TP} = 64$ thermopile detectors that are sensible in the $8 - 13 \mu\text{m}$ LWIR infrared band with a noise equivalent temperature difference of $\pm 0.08 \text{ }^\circ\text{C} @ 1 \text{ Hz}$ at room temperature. Each sensor acquires thermal IR images organized as 2D frames of 8×8 pixels [45].

Thermopile detectors independently measure the captured IR radiation and convert it to temperature readings that are the inputs of the data pipeline $i = 3$ (in Fig. 2)

$$\mathbf{X}_{k,3}(t) = [x_{k,t}(1), \dots, x_{k,t}(N_{TP})]. \quad (7)$$

Pre-processing of temperature readings is carried out to obtain the body-induced thermal signatures $\tilde{\mathbf{X}}_{k,3}(t) = f_3(\mathbf{X}_{k,3}|\phi_3 = [\mathbf{W}_k(\emptyset)])$ that measure the temperature increase as induced by body movements

$$\tilde{\mathbf{X}}_{k,3}(t) = \mathbf{X}_{k,3}(t) - \mathbf{W}_k(\emptyset) \quad (8)$$

where now $\mathbf{W}_k(\emptyset) = [x_{k,t}(1), \dots, x_{k,t}(N_{TP})]$ conveys information about stationary heat-sources (*i.e.*, robots, other machinery) that are not caused by body movements but characterize the background temperature of the empty space \emptyset . Computer vision methods [40] or statistical approaches [41] can be adopted to track body positions/motions. In Sect. V, we verify that fusion of such information with features obtained from THz radars is effective in improving worker motion discrimination in proximity with the robotic manipulator.

C. Multi-antenna installations for directional sensing and worker counting

Increasingly, multi-antenna systems are installed in WiFi and cellular settings. Such antenna-diversity techniques can be exploited in I4.0 scenarios, for instance, for simultaneous multi-target tracking, for worker counting, or for recognition of complex human contexts or activities. We assume here a scenario with a dedicated transmitter and a multi-antenna receiver in the direct LOS. Such installation might span a workplace scenario with multiple work locations. At the receiver side, various phase offsets of the RF-chains correspond to different steering angles of the recognition beams. It is thus possible to enable directional perception of the environment from multi-antenna omnidirectional devices. This angular information establishes evidence on the direction of body movement with respect to the antenna. At the same time, multiple beam analysis can further grant simultaneous multi-target recognition and tracking. This enables, for instance, the simultaneous tracking and monitoring of multiple body parts, as well as the counting of multiple subjects.

In what follows, we assume a WiFi installation featuring a multi-antenna receiver equipped with an antenna array with M elements that is connected to pipeline $i = 4$. The received signal at k -th antenna of the array ($k = 1, \dots, M$), namely the channel state information (CSI) $X_{k,4}(t)$, is composed [42] by the direct LOS signal $L_k(t)$, the signal $i_k(t)$ reflected by the target, as well as noise $n_k(t)$:

$$X_{k,4}(t) = L_k(t) + i_k(t) + n_k(t). \quad (9)$$

It is possible to amplify and isolate the desired signal $i_k(t)$ by applying proper beamforming weights $\mathbf{w} := \{w_k\}_{k=1}^M$ and by subsequently subtracting the estimated LOS signal $\tilde{L}_k(t)$ [43]. The de-noised sequence $\tilde{X}_{k,4}(t) = f_4(X_{k,4}|\phi_4 = [\mathbf{w}, \tilde{L}_k(t)])$ serves as an estimate of $i_k(t)$ and can be further processed to detect movements or activities. Repeated correction of the beamformer weights \mathbf{w} achieves mobile target tracking and activity recognition [42].

For a high recognition accuracy, it is beneficial to establish a small beam width. The beam width is naturally dictated by the count (M) of antennas at the receiver. In the presence of multiple targets (*e.g.*, multiple subjects or multiple moving

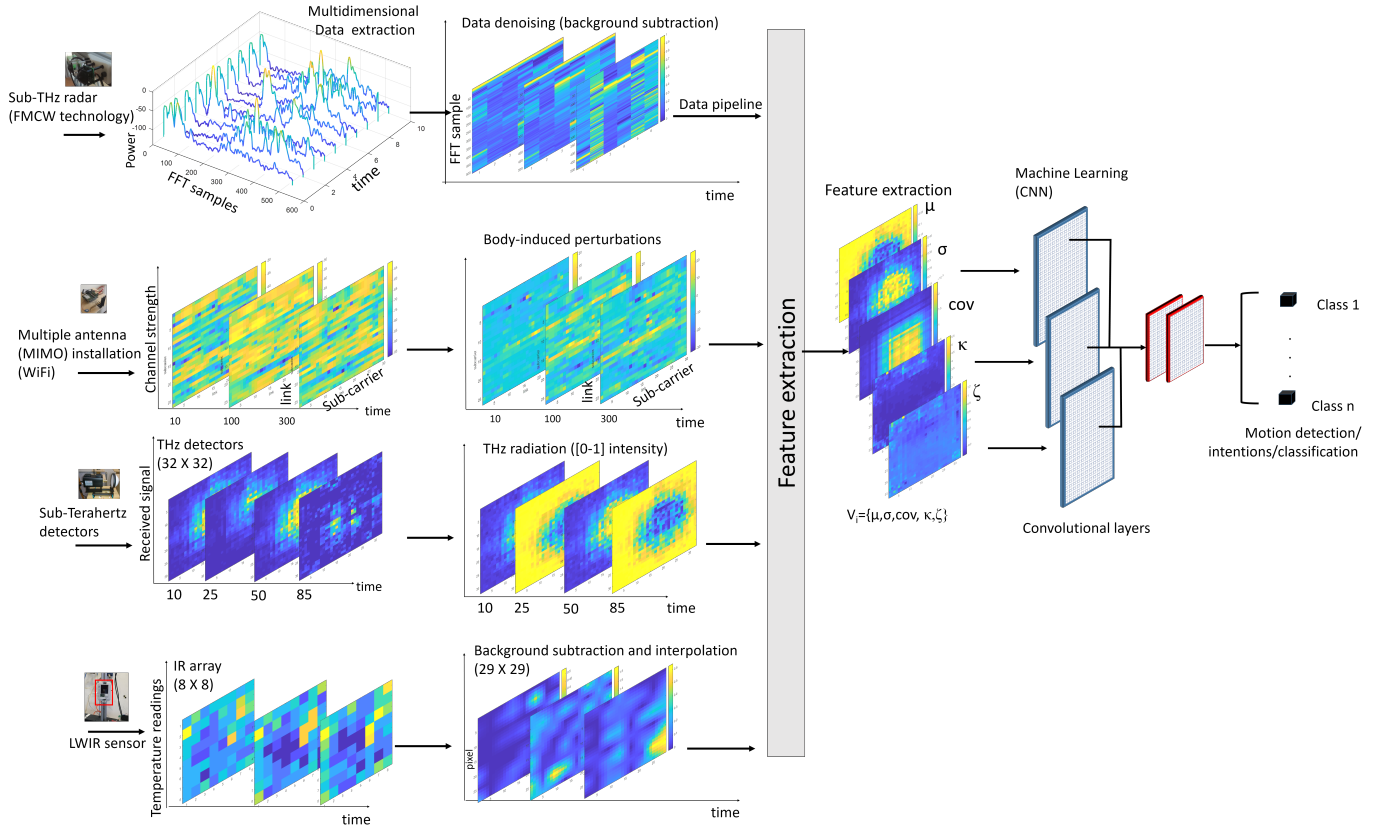


Fig. 5. MDF platform and data fusion examples. From left to right: raw data and feature extraction from 4 data pipelines (sub-THz radars at 122 GHz - FMCW technology, WiFi, sub-THz detectors at 100 GHz, and LWIR arrays), feature processing and classification.

body parts), isolation of distinct array responses for various directions yields separate information about these multiple targets and thus allows multi-subject or multi-target tracking [44]. It has been shown in [44], that proper clustering of this spatial streams can be used for crowd counting applications. In Sect. V, the worker counting system is implemented to monitor a passage room where workers move *e.g.* before entering the shared workspace.

V. EXPERIMENTAL VALIDATION AND CASE STUDIES

The proposed IoT MDF platform is validated through experimental activities inside a representative robotic cell [29]. In particular, we focused on 3 scenarios, each targeting a different HRC function:

- *Worker counting*: In Sect. V-A, we tackle the problem of counting the number of workers present in a monitored passage room of size 5.5 m x 4 m by exploiting directional information on signal perturbations, obtained from multi-antenna instrumentation (pipeline $i = 4$, Sect. IV-C). The system employs training-free techniques and thus it is robust to changing environments.
- *Worker motion detection*: Sect. V-B addresses the problem of worker motion detection inside the *operating space* (approx. $d > 1$ m from the robot) of the robotic cell and for different positions of the worker. The corresponding layout is detailed in Fig. 4.a,b. The proposed MDF platform applies feature fusion by using sub-THz

radars (pipeline $i = 1$) and sub-THz detectors ($i = 2$). The scenario is effective in many SSM tasks as shown in Sect. II-A.

- *Worker-Robot co-presence monitoring*: Sect. V-C addresses the critical case of human-robot workflow monitoring inside the *shared space* and during a collaborative task that requires the worker and the robotic manipulator to cooperate at close distance ($d < 1$ m). The corresponding layout is detailed in Fig. 4.c and 4.d. For this case, the platform combines both sub-THz radar sensors ($i = 1, 2$) and IR array devices ($i = 3$) that are re-used here opportunistically to track the worker motion intentions and occupancy (*i.e.*, position) inside the working area.

The collaborative setup is composed by a robotic manipulator from Universal Robot UR10, with 10 kg payload mounted on a workdesk. Robot tasks are pick-and-place activities: the robot picks objects from an inbound conveyor and moves them to a outbound bin. In the meantime, the operator picks the objects that require addition work, such as disassembling or re-manufacturing.

As shown in Fig. 5, the IoT MDF platform consists of $N = 4$ selectable pipelines described in Sect. IV, namely: *i*) 6 FMCW radars (Sect. IV-A); *ii*) a sub-THz source and camera (Sect. IV-B) implementing a virtual fence system; *iii*) 3 IR array sensors, with one of them ceiling-mounted; and *iv*) 3 software-defined radio devices to test worker counting functions (Sect. V-A). Sensors continuously monitor the area by

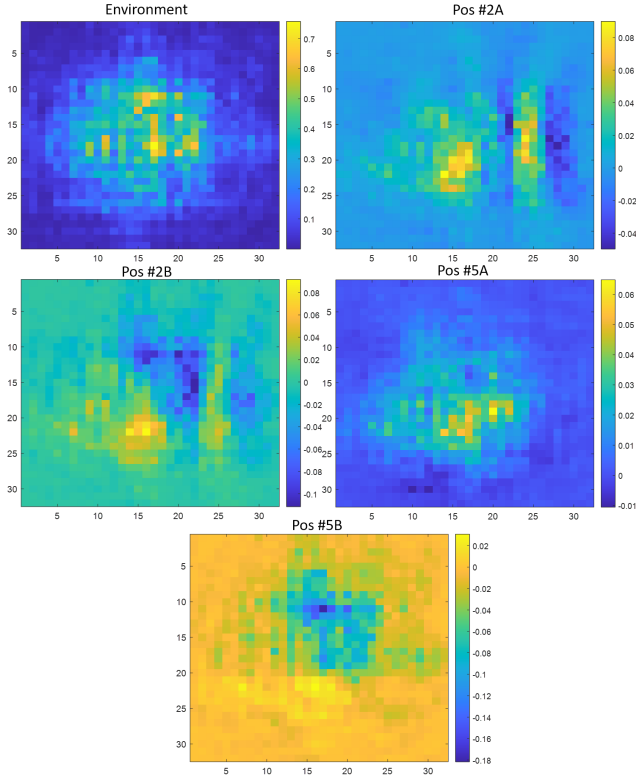


Fig. 6. Image of human body movements captured by sub-THz detector array at the predefined locations mentioned in layout in Fig. 4. Position number at images corresponds to predefined locations A/B correspond to human body wo/w body movements, respectively.

collecting raw data and forwarding them to the corresponding micro-edge server. For data distribution, FMCW radars and sub-THz cameras use a 2.4 GHz WiFi link, while IR sensors send the data to an intermediate access point (AP) using an IEEE 802.15.4e implementation [17], the AP forwards the aggregated data to the edge via 2.4GHz WiFi. The edge node extracts and sends the features to the cloud for classification (Sect. III). Features are transferred through MQTT messages in real-time using a wired transport network (Ethernet), but optimized for safety [20].

A data controller handles the orchestration of features: it can therefore decide how many pipelines should be combined inside the edge depending on the required HRC function. For example, occupancy detection inside the operating space does not require high accuracy, considering that the worker is operating at safe distance from the robot. It could be obtained using only a couple of data pipelines to minimize latency. On the contrary, co-presence monitoring requires higher accuracy, therefore features must be selected considering the latency-accuracy trade-off and the protective distance d_p evaluation. In what follows, both non-cooperative sensing, that uses the individual pipelines separately, and cooperative sensing, that adopts the fusion of features, are discussed and compared using boht CNN and LSTM models.

TABLE I
WORKER COUNTING CONFUSION MATRIX. ACTUAL VS. ESTIMATED COUNT (% AND #) IN AN INDOOR CONFINED AREA OF 5.6 M X 4.0 M.

	Estimated worker count % (#)				
	0	1	2	3	4
0	100% (12)				
1		89% (16)	11% (2)		
2		3% (1)	47% (14)	47% (14)	3% (1)
3			5.5% (1)	89% (16)	5.5% (1)

A. Worker counting

The first use case focuses on the worker counting problem using features from pipeline $i = 4$ and obtained from a multi-antenna radio installation. To this aim, in an indoor area of 5.5 m x 4.0 m, we installed a dedicated transmitter (USRP X300 series with UBX-160 and SBX RF-daughterboard) centered at one of the longer walls and a four-antenna receiver ($M = 4$) centered on the opposite wall. Another USRP is installed in the corner of the area and used to synchronize with the Rx USRPs by broadcasting a reference signal to calibrate each RX frame offset. Clock coherence at each USRP Rx has been achieved via a clock distribution system, which provided a pulse-per-second and a 10 MHz reference signal to discipline the local oscillators. This OFDM system operated at 3.42 GHz with a bandwidth of 15.32 MHz into which 5408 subframes (each 3082 samples long) are established over 52 usable subcarriers.

A total of 6 different people participated in the experiment and conducted dedicated movements at up to 12 confined locations. Table I summarizes the results for 0-3 persons². We estimate the worker count within an error of 1 for up to 4 persons. Results were achieved in a training-free manner so that the system is robust against frequent environmental changes or also to re-location. In particular, this is useful to meet the high demands of frequently and dynamically changing industrial workplace settings. In particular, we detect workers via beam scanning in which the direction of arrival for reflected and LOS signals create a distribution over time. For environments with multiple workers present, the resulting mixture of several Gaussian distributions is separated by a clustering approach. We exploit joint approximate diagonalization of eigen-matrices (JADE) [48] for blind source separation of the observed, only partially orthogonal streams. We derive a distance matrix \mathbf{D} between the respective streams by applying constrained derivative dynamic time warping (cDDTW) [49]. As clustering method, we have chosen Hierarchical agglomerative clustering (HAC) [50], using the distance matrix \mathbf{D} .

The above approach is able to recognize the presence of workers in distinct spatial streams. Since the amplitude fluctuation from neighboring streams is smaller than the one caused by a person in that spatial stream, noise and interference from neighboring locations are small and hence the recognition accuracy improved. However, in our case studies, noise and interference from neighboring locations are not completely erased by the approach. Instead, some correlation remains and it is particularly pronounced when the respective neighboring cell is empty. In such case, false positives are likely and have to

²The worker count is limited by the number of antennas utilized [44]

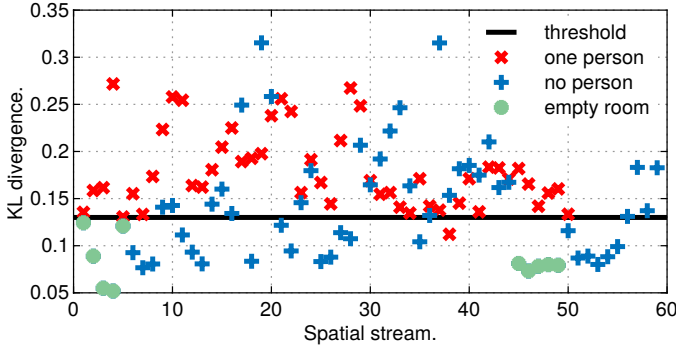


Fig. 7. Kullback-Leibner divergence of the detection of human absence in spatial streams.

be separately addressed by analyzing the correlation between spatial streams with predicted worker presence.

To show this, we computed the Kullback-Leibner divergence for pairs of neighboring spatial streams where either: *i*) no worker was present in all spatial streams (namely *empty room*), *ii*) the stream was occupied by a worker (namely, *one person*), and *iii*) the stream was not occupied but a neighboring stream was (namely, *no person*). Fig. 7 depicts the Kullback-Leibner divergence for these samples.

The empty room is well distinguished from the other cases, as most remain below the Kullback-Leibner threshold, and also the majority of cases with *one person* in the spatial stream are well above the threshold. However, the cases with no person next to a stream that is occupied by a person are not clearly distinguished and hence are a potential source for false positives. To avoid this one-sided error, we suggest to employ a correlation analysis over all spatial streams. In fact, high correlation among neighboring streams indicates likely false positives.

B. Worker detection inside the operating space ($d > 1$ m)

The second scenario focuses on the robotic cell of Fig. 4.a and tests the performance of worker motion detection and localization in the landmark positions 1 up to 6 inside the operating space of the manipulator with distance $d > 1$ m from the robot. Since the worker, even when standing, is not rigid but moves around each landmark, the 6 positions correspond to 8 different body postures: 1, 2A, 2B, 3, 4, 5A, 5B, 6 as marked in the figure. For example, the worker at position number 2 implements two different postures: 2A relates to the worker standing at position 2 and moving in the surroundings, 2B corresponds to a worker performing simple pick-and-place activities in the surrounding of the assembly line. Likewise, the same postures are used also in position 5. In what follows, we analyze at first, the system performance considering the processing of the FMCW radar features V_1 (pipeline $i = 1$) and the sub-THz detector ones V_2 (pipeline $i = 2$) separately. Next, sensor fusion is evaluated by merging the features V_1 , V_2 and running ML on the cloud back-end.

Fig. 5 on top shows an example of radar FFT samples obtained from 6 FMCW sensors working in the 122 GHz band inside the monitoring area. FFT samples are processed as in

		Input features: V_2 (sub-THz detectors)								
		Confusion Matrix								
Output class	1	2A	2B	3	4	5A	5B	6		
	1	11 6.9%	1 0.6%	0 0.0%	2 1.3%	4 2.5%	2 1.3%	0 0.0%	2 1.3%	50.0% 50.0%
2A	2 1.3%	16 10.0%	6 3.8%	3 1.9%	2 1.3%	4 2.5%	0 0.0%	3 1.9%	40.0% 60.0%	
2B	0 0.0%	0 0.0%	8 5.0%	0 0.0%	0 0.0%	2 1.3%	4 2.5%	1 0.6%	53.3% 46.7%	
3	4 2.5%	3 1.9%	0 0.0%	13 8.1%	5 3.1%	1 0.6%	0 0.0%	1 0.6%	48.1% 51.9%	
4	3 1.9%	0 0.0%	0 0.0%	0 0.0%	8 5.0%	1 0.6%	0 0.0%	1 0.6%	61.5% 38.5%	
5A	0 0.0%	0 0.0%	0 0.0%	0 0.0%	1 0.6%	10 6.3%	0 0.0%	0 0.0%	90.9% 9.1%	
5B	0 0.0%	0 0.0%	6 3.8%	0 0.0%	0 0.0%	0 0.0%	15 9.4%	3 1.9%	62.5% 37.5%	
6	0 0.0%	0 0.0%	0 0.0%	0 0.0%	0 0.0%	0 0.0%	1 0.6%	7 4.4%	87.5% 12.5%	
	Recall	55.0%	80.0%	40.0%	65.0%	40.0%	50.0%	75.0%	35.0%	
	False negative rate	45.0%	20.0%	60.0%	35.0%	60.0%	50.0%	25.0%	65.0%	
		1	2	3	4	5	6			
		1	2	3	4	5	6			

		Input features: V_1 (THz radars)								
		Confusion Matrix								
Output class	1	2A	2B	3	4	5A	5B	6		
	1	40 12.5%	0 0.0%	1 0.3%	0 0.0%	0 0.0%	0 0.0%	0 0.0%	1 0.3%	95.2% 4.8%
2A	0 0.0%	39 12.2%	15 4.7%	3 0.9%	1 0.3%	1 0.3%	1 0.3%	0 0.0%	61.9% 38.1%	
2B	0 0.0%	1 0.3%	19 5.9%	0 0.0%	0 0.0%	2 0.6%	1 0.3%	1 0.3%	79.2% 20.8%	
3	0 0.0%	0 0.0%	1 0.3%	33 10.3%	0 0.0%	0 0.0%	0 0.0%	0 0.0%	97.1% 2.9%	
4	0 0.0%	0 0.0%	0 0.0%	0 0.0%	38 11.9%	1 0.3%	0 0.0%	0 0.0%	97.4% 2.6%	
5A	0 0.0%	0 0.0%	1 0.3%	0 0.0%	0 0.0%	15 4.7%	2 0.6%	1 0.3%	78.9% 21.1%	
5B	0 0.0%	0 0.0%	3 0.9%	1 0.3%	18 5.6%	36 11.3%	5 1.6%	5 1.6%	53.7% 46.3%	
6	0 0.0%	0 0.0%	0 0.0%	0 0.0%	0 0.0%	0 0.0%	0 0.0%	32 10.0%	100% 0.0%	
	Recall	100%	97.5%	47.5%	82.5%	95.0%	37.5%	90.0%	80.0%	
	False negative rate	0.0%	2.5%	52.5%	17.5%	5.0%	62.5%	10.0%	20.0%	
		1	2	3	4	5	6			
		1	2	3	4	5	6			

Fig. 8. Confusion matrix results for LSTM networks for worker detection. Top: performances using only feature V_2 from sub-THz detectors (pipeline $i = 2$) without data fusion; bottom: performances using only feature V_1 from FMCW radars (pipeline $i = 1$) without data fusion. The classes correspond to 8 activities of a worker at 6 predefined positions.

equation (4) from pipeline $i = 1$ inside the edge to extract the features V_1 in (2). Features are then arranged and interpolated to fit with the required 2D ML model input size and sent to the ML stages running in the cloud.

Likewise, considering now pipeline $i = 2$, the radiation intensity obtained from the sub-THz camera is altered by the presence of the worker in the surroundings of the assembly line. This is visualized in Fig. 6, where we highlight the measured radiation obtained from the sub-THz camera arranged as a 2D matrix of 32×32 equivalent pixels in correspondence of the empty environment and when the worker is located at positions 2A, 2B, 5A and 5B. The sub-THz camera is reused opportunistically to detect and discriminate worker motions in the surroundings of the assembly line. A worker approaching the assembly line affects the received sub-THz radiation: the radiation intensity changes are more significant at positions 2B and 5B, compared with postures at 2A and 5A, due to the movements of the worker arms, in addition to the torso.

At the cloud back-end, LSTM and CNN tools are compared for position/activity classification. In particular, the CNN model captures recurring structures from the input 2D features using spatially located convolutional filters. On the contrary, the LSTM network monitors long and short-term

Input features: V_2 (sub-THz detectors)

Confusion Matrix

1	609	2	0	2	37	0	0	0	93.7%
	11.7%	0.0%	0.0%	0.0%	0.7%	0.0%	0.0%	0.0%	6.3%
2A	0	548	85	17	0	0	0	0	84.3%
	0.0%	10.5%	1.6%	0.3%	0.0%	0.0%	0.0%	0.0%	15.7%
2B	0	7	621	0	0	0	22	0	95.5%
	0.0%	0.1%	11.9%	0.0%	0.0%	0.0%	0.4%	0.0%	4.5%
3	9	0	0	584	57	0	0	0	89.8%
	0.2%	0.0%	0.0%	11.2%	1.1%	0.0%	0.0%	0.0%	10.2%
4	23	0	0	0	627	0	0	0	96.5%
	0.4%	0.0%	0.0%	0.0%	12.1%	0.0%	0.0%	0.0%	3.5%
5A	0	0	0	0	0	580	70	0	89.2%
	0.0%	0.0%	0.0%	0.0%	0.0%	11.2%	1.3%	0.0%	10.8%
5B	0	0	1	0	0	3	646	0	99.4%
	0.0%	0.0%	0.0%	0.0%	0.0%	0.1%	12.4%	0.0%	0.6%
6	0	0	0	0	0	0	0	650	100%
	0.0%	0.0%	0.0%	0.0%	0.0%	0.0%	0.0%	12.5%	0.0%
Recall	95.0%	98.4%	87.8%	96.8%	87.0%	99.5%	87.5%	100%	93.6%
False negative rate	5.0%	1.6%	12.2%	3.2%	13.0%	0.5%	12.5%	0.0%	6.4%
Overall accuracy									6.4%

Target Class

Input features: V_1, V_2 (THz radars, detectors)

Confusion Matrix

1	20	0	0	0	0	0	0	0	100%
	12.5%	0.0%	0.0%	0.0%	0.0%	0.0%	0.0%	0.0%	0.0%
2A	0	19	0	0	0	0	0	0	100%
	0.0%	11.9%	0.0%	0.0%	0.0%	0.0%	0.0%	0.0%	0.0%
2B	0	1	20	0	0	0	0	0	95.2%
	0.0%	0.6%	12.5%	0.0%	0.0%	0.0%	0.0%	0.0%	4.8%
3	0	0	0	19	0	0	0	0	100%
	0.0%	0.0%	0.0%	11.9%	0.0%	0.0%	0.0%	0.0%	0.0%
4	0	0	0	0	20	0	0	0	100%
	0.0%	0.0%	0.0%	0.0%	12.5%	0.0%	0.0%	0.0%	0.0%
5A	0	0	0	1	0	20	0	0	95.2%
	0.0%	0.0%	0.0%	0.6%	0.0%	12.5%	0.0%	0.0%	4.8%
5B	0	0	0	0	0	0	17	0	100%
	0.0%	0.0%	0.0%	0.0%	0.0%	0.0%	10.6%	0.0%	0.0%
6	0	0	0	0	0	0	3	20	87.0%
	0.0%	0.0%	0.0%	0.0%	0.0%	0.0%	1.9%	12.5%	13.0%
Recall	100%	95.0%	100%	95.0%	100%	100%	85.0%	100%	96.9%
False negative rate	0.0%	5.0%	0.0%	5.0%	0.0%	0.0%	15.0%	0.0%	3.1%
Overall accuracy									3.1%

(a) LSTM

Input features: V_1 (THz radars)

Confusion Matrix

1	400	0	0	0	0	0	0	0	100%
	12.5%	0.0%	0.0%	0.0%	0.0%	0.0%	0.0%	0.0%	0.0%
2A	0	378	22	0	0	0	0	0	94.5%
	0.0%	11.8%	0.7%	0.0%	0.0%	0.0%	0.0%	0.0%	5.5%
2B	0	0	400	0	0	0	0	0	100%
	0.0%	0.0%	12.5%	0.0%	0.0%	0.0%	0.0%	0.0%	0.0%
3	0	0	0	398	0	2	0	0	99.5%
	0.0%	0.0%	0.0%	12.4%	0.0%	0.1%	0.0%	0.0%	0.5%
4	0	0	0	0	400	0	0	0	100%
	0.0%	0.0%	0.0%	0.0%	12.5%	0.0%	0.0%	0.0%	0.0%
5A	0	0	0	0	0	378	22	0	94.5%
	0.0%	0.0%	0.0%	0.0%	0.0%	11.8%	0.7%	0.0%	5.5%
5B	0	0	0	0	0	15	371	14	92.8%
	0.0%	0.0%	0.0%	0.0%	0.0%	0.5%	11.6%	0.4%	7.3%
6	0	0	0	0	0	0	1	399	99.8%
	0.0%	0.0%	0.0%	0.0%	0.0%	0.0%	0.0%	12.5%	0.2%
Recall	100%	100%	94.8%	100%	100%	95.7%	94.2%	96.6%	97.6%
False negative rate	0.0%	0.0%	5.2%	0.0%	0.0%	4.3%	5.8%	3.4%	2.4%
Overall accuracy									2.4%

Target Class

Input features: V_1, V_2 (THz radars, detectors)

Confusion Matrix

1	698	0	0	0	0	0	0	0	99.7%
	12.5%	0.0%	0.0%	0.0%	0.0%	0.0%	0.0%	0.0%	0.3%
2A	2	550	142	0	2	0	0	4	78.6%
	0.0%	9.8%	2.5%	0.0%	0.0%	0.0%	0.0%	0.1%	21.4%
2B	2	0	696	2	0	0	0	0	99.4%
	0.0%	0.0%	12.4%	0.0%	0.0%	0.0%	0.0%	0.0%	0.6%
3	1	0	0	695	1	1	2	0	99.3%
	0.0%	0.0%	0.0%	12.4%	0.0%	0.0%	0.0%	0.0%	0.7%
4	0	0	0	0	700	0	0	0	100%
	0.0%	0.0%	0.0%	0.0%	12.5%	0.0%	0.0%	0.0%	0.0%
5A	0	0	0	0	0	649	51	0	92.7%
	0.0%	0.0%	0.0%	0.0%	0.0%	11.6%	0.9%	0.0%	7.3%
5B	0	0	6	10	3	54	597	30	85.3%
	0.0%	0.0%	0.1%	0.2%	0.1%	1.0%	10.7%	0.5%	14.7%
6	0	0	0	0	0	0	0	700	100%
	0.0%	0.0%	0.0%	0.0%	0.0%	0.0%	0.0%	12.5%	0.0%
Recall	99.3%	100%	82.5%	98.3%	99.2%	91.9%	91.8%	95.4%	94.4%
False negative rate	0.7%	0.0%	17.5%	1.7%	0.8%	8.1%	8.2%	4.6%	5.6%
Overall accuracy									5.6%

(b) CNN

Fig. 9. Confusion matrix results for CNN networks for worker detection. Top: performances using only feature V_2 from sub-THz detectors (pipeline $i = 2$) without data fusion; bottom: performances using only feature V_1 from FMCW radars (pipeline $i = 1$) without data fusion. The classes correspond to the 8 activities of a worker at 6 predefined positions.

Fig. 10. Confusion matrix results for worker detection using fused features V_1 and V_2 from both FMCW radars (pipeline $i = 1$) and the sub-THz camera (pipeline $i = 2$). Top: LSTM performances; bottom: CNN performance. The classes correspond to the 8 activities of a worker at 6 predefined positions.

correlations over the feature samples, arranged similarly as for CNN. LSTM consists of an individual trainable layer of 8 units and 8 softmax outputs to track the corresponding worker positions. The CNN model uses 2D input features of size (32×32) and consists of 3 trainable layers: it is detailed in Table II (for the case $d > 1$ m). Both non-cooperative and cooperative sensing cases use the same ML model. Note that, when fusing both features V_1 and V_2 , input size adaptations are required to fit with 32×32 2D dimensions, *e.g.* by interpolation/decimation and reshaping. In addition, convolutional filters run independently for each feature/pipeline: a flattening layer (see also Fig. 5) is used to collapse the convolutional filter output dimensions so that the outputs can be processed by the FC layer. In all cases, 80% of data is used for training and 20% for real-time classification.

Figs. 8 and 9 show the confusion matrix (precision, recall, and overall accuracy) obtained with LSTM and CNN, respectively. Each tool uses individual features V_1 and V_2 as inputs without implementing any data fusion (non-cooperative sensing). Fig. 8 on top shows the performance of the sub-THz camera system ($i = 2$) while the bottom one shows

the corresponding confusion matrix results obtained using the FMCW radars ($i = 1$). Processing of features V_1 gives better accuracy results, (*i.e.*, 78.8%) with respect to V_2 (*i.e.*, 55%). In Fig. 9, we now employed the CNN model by analyzing, again separately, the features V_1 and V_2 . We noticed that CNN outperforms LSTM since both features are more spatially- than time-correlated.

In Fig. 10, the detection system fuses both features V_1 and V_2 using data normalization techniques based on the min-max approach [30]. Fig. 10 shows the confusion matrices for both LSTM and CNN. Results confirm the expected improvements of the cooperative approach that jointly operated on both V_1 and V_2 features. In fact, the accuracy increases to 96.9% and 94.4% for CNN and LSTM, respectively.

In what follows, the CNN model is chosen for protective distance d_p and quantitative evaluation of robustness (Sect. VI).

		Input features: V_3 (IR array)						Input features: V_1, V_2, V_3 (THz radars, detectors, IR array)					
		Confusion Matrix						Confusion Matrix					
Output class	C	334 15.5%	65 3.0%	7 0.3%	0 0.0%	11 0.5%	80.1% 19.9%	415 19.3%	5 0.2%	5 0.2%	0 0.0%	9 0.4%	95.6% 4.4%
	D	66 3.1%	282 13.1%	12 0.6%	0 0.0%	0 0.0%	78.3% 21.7%	7 0.3%	423 19.7%	4 0.2%	0 0.0%	0 0.0%	97.5% 2.5%
	A	8 0.4%	24 1.1%	405 18.8%	0 0.0%	0 0.0%	92.7% 7.3%	5 0.2%	14 0.7%	406 18.9%	0 0.0%	0 0.0%	95.5% 4.5%
	B	0 0.0%	0 0.0%	0 0.0%	430 20.0%	0 0.0%	100% 0.0%	0 0.0%	0 0.0%	0 0.0%	430 20.0%	0 0.0%	100% 0.0%
	E	26 1.2%	63 2.9%	0 0.0%	0 0.0%	418 19.4%	82.4% 17.6%	4 0.2%	0 0.0%	0 0.0%	0 0.0%	424 19.7%	99.1% 0.9%
		77.0% 23.0%	65.0% 35.0%	95.5% 4.5%	100% 0.0%	97.4% 2.6%	86.9% 13.1%	96.3% 3.7%	95.7% 4.3%	97.8% 2.2%	100% 0.0%	97.9% 2.1%	97.5% 2.5%
		Target Class						Target Class					

Fig. 11. Confusion matrix results for worker-robot co-presence monitoring. Left: CNN performance without data fusion using only feature V_3 from the IR array (pipeline $i = 3$). Right: CNN performance with data fusion using features V_1, V_2 , and V_3 from FMCW radars, the sub-THz camera, and the IR array (pipelines $i = 1, 2, 3$), respectively.

TABLE II

FEATURES INPUT SIZES AND ML MODEL LAYERS FOR DETECTION INSIDE THE OPERATING ($d > 1$ M) AND THE COLLABORATIVE ($d < 1$ M) SPACES.

	Selected features	Feature input size	ML model layers (CNN)			
$d > 1m$	$V_1 = \{\mu_{1,k}\}_{k=1}^{1024}$ $V_2 = \{\sigma_{2,k}\}_{k=1}^{1024}$	$V_1: 512 \times 6$ (reshaped to 32×32 by decimation) $V_2: 32 \times 32$	$V_1: 32 \times 32$ 16 2D conv. (3x3) Relu + pooling 32 2D conv. (3x3) Relu + pooling	$V_2: 32 \times 32$ 16 2D conv. (3x3) Relu + pooling 32 2D conv. (3x3) Relu + pooling		
			Flatten layer FC (Fully Connected) Regression (8 outputs)			
$d < 1m$	$V_1 = \{\mu_{1,k}\}_{k=1}^{1024}$ $V_2 = \{\sigma_{2,k}\}_{k=1}^{64}$ $V_3 = \{\mu_{3,k}\}_{k=1}^{64}$	$V_1: 512 \times 6$ (reshaped to 32×32 by segmentation) $V_2: 32 \times 32$ $V_3: 8 \times 8$ (reshaped to 32×32 by interpolation)	$V_1: 32 \times 32$ 16 2D conv. (3x3) Relu + pooling	V_2 \vdots	V_3 \vdots	
			Flatten layer FC + Softmax Classification (5 outputs)			

C. Worker-robot co-presence monitoring ($d < 1$ m)

In the third use case, we verified the performance of the proposed MDF platform with respect to its ability to recognize the worker in the critical landmarks A, B, C, D and E inside the collaborative space (see Fig. 4.c and 4.d). As seen before, the performance analysis is based on the comparison of the confusion matrices to assess precision, recall and average accuracy metrics. The motion detection system inside the collaborative space must be now more accurate compared with the previous case as monitoring critical co-presence situations. Features V_1, V_2 , and V_3 obtained from the FMCW radars (pipeline $i = 1$), the sub-THz detectors ($i = 2$) and the IR arrays ($i = 3$) are thus fused together.

In Fig. 11, we verified the detection accuracy in the selected positions using the IR array alone (Fig. 11.a) and by fusing all the features V_1, V_2 , and V_3 (Fig. 11.b). In both cases, we adopt a CNN model with parameters illustrated in Tab. II (for $d < 1$ m). Similarly as done in the previous section, when fusing all the features V_1, V_2 , and V_3 , the 3 inputs are converted to 2D data structures of similar size. Each 2D

structure serves as input to the corresponding convolutional filter. Filter outputs are flattened being the inputs of a FC layer to classify up to 6 HR co-presence situations. Data fusion substantially improves the detection performance: considering the average accuracy, it increases from 86.9% to 97.5%. Similar improvements are observed in terms of precision and recall for all landmarks.

VI. MDF PLATFORM ROBUSTNESS FOR HUMAN-ROBOT COLLABORATION SCENARIOS

In this section, we focus more specifically on the analysis of the MDF system robustness. Considering the HRC environment and the related risk mitigation policies, robustness is quantified here in terms of the minimum *protective separation distance* d_p . Distance d_p provides a standardized indicator of the minimum human-robot separation below which the robot must stop or replan its activities. Increasing HR separation makes the system more robust to inaccuracies; however, it reduced HRC workspace efficiency. In what follows, we focus on a typical SSM operation scheme (Sect. II-A) where the robot(s) and the operator(s) may move concurrently in the shared workspace. As shown in Sect. VI-A, the protective distance d_p is underpinned by the worker localization uncertainties as well as ML-based detection/classification latencies. In Sect. VI-B, localization accuracy and latency of the MDF platform are measured to analyze the minimum protective distance for different manipulator speeds. Maximum robot speed and localization uncertainties can be traded to minimize d_p and thus improving system robustness.

A. Protective human-robot separation distance

The protective human-robot separation distance is defined [25] as the shortest permissible distance d_p between any moving parts of the robot and any human in the collaborative workspace. The robot is *safety-rated* programmed so that it never gets closer to the operator than d_p by lowering its speed, while if this happens due to operator unsafe motions, the robot system must protectively stop. The protective distance depends also on the robot speed v_r and the relative position of the worker. It is thus affected by the uncertainty factors related to the detection/classification process. Considering the standard [25], the general equation for d_p , at time t_0 , can be expressed as

$$d_p(t_0) = \int_{t_0}^{t_0+T_w+T_r+T_s} v_w(t) dt + \int_{t_0}^{t_0+T_w+T_r} v_r(t) dt + \int_{t_0+T_w+T_r}^{t_0+T_w+T_r+T_s} v_s(t) dt + Z_r + Z_w \quad (10)$$

where we have indicated the instantaneous velocity terms $v_w(t)$, $v_r(t)$ and $v_s(t)$ (expressed in m/s) that refer to the directed speed of the worker (moving in the direction of the robot), the directed speed of the robot (in the direction of the worker) and directed speed of the robot while stopping, respectively. T_w refers to the worker detection latency (in seconds), T_r indicates the time interval needed to activate the robot stop command while T_s describes the time interval required to completely stop the robot. The worker and

robot detection uncertainty factors Z_w, T_w and Z_r correspond to: *i*) the worker localization accuracy Z_w (in meters); *ii*) the worker detection latency T_w (in seconds); and *iii*) the robot localization accuracy Z_r (in meters). In particular, the overall reaction time of the robot system, is the sum of the required time T_w for the detection of the worker, that includes data collection and edge/cloud processing, the activation of robot stop T_r , and, finally, the time T_s the robot takes to stop its movements.

In what follows, we assume $Z_r \ll Z_w$; in addition, we use the maximum worker/robot speed values $v_w \leq v_w(t)$, $v_r \leq v_r(t)$ and the average speed $v_s = \mathbb{E}_t[v_s(t)]$ of the robot during the stopping phase. By implicitly dropping the current time t_0 , the previous equation can be rewritten as

$$d_p = v_w \times (T_w + T_r + T_s) + v_r (T_w + T_r) + v_s T_s + Z_w. \quad (11)$$

Therefore, d_p is a function of the worker detection uncertainty factors Z_w, T_w , while the other parameters are defined in Tab. III. The localization accuracy Z_w and the detection latency T_w are thus ruled by the proposed MDF platform and are evaluated in the following section.

B. Latency and accuracy analysis from cases studies

In Tab. IV, the accuracy Z_w and the detection latency T_w are measured separately for the detection of worker at distance $d > 1$ m from the robot and the human-robot co-presence at $d < 1$ m. The localization accuracy Z_w is obtained for varying landmarks, according to the deployment of Fig. 4, namely the positions 1, 2, ..., 5 for $d > 1$ m and positions A, B, ..., E for $d < 1$ m. The average accuracy is $Z_w = 0.54$ m for $d > 1$ m and $Z_w = 0.28$ m for $d < 1$ m, respectively.

The latency T_w of the MDF platform corresponds to the time interval between the pre-processing of raw data on the edge and the ML based classification of the fused features on the cloud. Latency thus depends on the number of pipelines that are needed by the cloud to process the new location update. More specifically, the worker localization for $d > 1$ m uses 2 pipelines: one consecutive FFT measurement $X_{k,1}(t)$ obtained from the 6 FMCW radars and one $X_{k,2}(t)$ measurement for each THz detector. The measured latency is $T_w = 37$ ms. On the contrary, co-presence monitoring for $d < 1$ m requires larger localization accuracy: the edge now combines 3 pipelines, namely 3 consecutive FMCW radar measurements $X_{k,1}(t)$, one $X_{k,2}(t)$ measurement for each THz detector and one thermal image $X_{k,3}(t)$. The need for a larger accuracy causes an increase of the latency to $T_w = 90$ ms.

Considering the robotic cell parameters in Tab. III, and the uncertainties Z_w, T_w , the protective human-robot separation distance has been computed in the Tab. IV using (11) for $d > 1$ m and $d < 1$ m, respectively. Assuming a constant manipulator speed set to a maximum value of $v_r = 0.5$ m/s, the separation distance is evaluated as $d_p = 0.83$ m for the operator located in the operating space ($d > 1$ m) and as $d_p = 0.63$ m for co-presence monitoring ($d < 1$ m), respectively. Decreasing the manipulator speed to $v_r = 0.15$ m/s counterbalances the larger reaction time ($T_w = 90$ ms) for

TABLE III
ROBOTIC CELL PARAMETERS FOR PROTECTIVE HUMAN-ROBOT SEPARATION DISTANCE d_p COMPUTATION.

Robotic cell parameters (for distance d_p computation)	
Maximum worker speed	$v_w = 0.5\text{m/s}$
Manipulator stopping speed	$v_s = 0.5\text{m/s}$
Manipulator speed	$v_r = 0.5\text{m/s}, v_r = 0.15\text{m/s}$
Manipulator stopping time	$T_s = 250\text{ms}$
Manipulator stop activation time	$T_r = 20\text{ms}$

TABLE IV
ANALYSIS OF UNCERTAINTY FACTORS AND PROTECTIVE HUMAN-ROBOT SEPARATION DISTANCE d_p : LOCALIZATION ACCURACY AND LATENCY FOR WORKER MOTION DETECTION ($d > 1$ M AS IN FIG. 4.B) AND WORKER-ROBOT CO-PRESENCE MONITORING ($d < 1$ M AS IN FIG. 4.D).

Worker motion detection				
	Worker positions (Fig. 4.b)	Localization accuracy [m]	Average Latency Fusion: V_1, V_2	
				$T_w = 37\text{ms}$ (1 FFT per localization update)
$d > 1$ m	1	$Z_w = 0.51$	Protective HR distance d_p vs. manipulator speed v_r	
	2	$Z_w = 0.52$		
	3	$Z_w = 0.51$		
	4	n.a.	$d_p = 0.83\text{m}$	$d_p = 0.82\text{m}$
	5	$Z_w = 0.62$	$v_r = 0.5\text{m/s}$	$v_r = 0.15\text{m/s}$
	6	n.a.		
Worker-robot co-presence monitoring				
	Worker positions (Fig. 4.d)	Localization accuracy [m]	Average Latency Fusion: V_1, V_2, V_3	
				$T_w = 90\text{ms}$ (1 thermal image + 3 FFT per localization update)
$d < 1$ m	A	$Z_w = 0.27$	Protective HR distance d_p vs. manipulator speed v_r	
	B	$Z_w = 0.25$		
	C	$Z_w = 0.28$		
	D	$Z_w = 0.33$	$d_p = 0.63\text{m}$	$d_p = 0.59\text{m}$
	E	$Z_w = 0.27$	$v_r = 0.5\text{m/s}$	$v_r = 0.15\text{m/s}$

co-presence monitoring ($d < 1$ m) as the protective distance now reduces from $d_p = 0.63$ m to $d_p = 0.59$ m. Decreasing robot speed when $d > 1$ m has instead a negligible impact on the protective distance as this is ruled by localization accuracy.

VII. CONCLUDING REMARKS AND OPEN PROBLEMS

We proposed a multisensor data fusion (MDF) edge-cloud platform using radio signals for opportunistic and anonymous perception of workers inside a cobot dynamic environment. The MDF platform integrates radio sensing technologies, ranging from infrared, WiFi to sub-THz IoT devices, and is deployed to monitor a fence less human-robot shared workplace, envisioned in Industry 4.0. We proposed a practical solution for the joint analysis of features based on machine learning techniques. In addition, we quantified and discussed the impact of detection uncertainties, namely accuracy and latency, on safe cooperation. The robustness of the MDF system is ruled by the protective human-robot separation distance that we quantified for different human-robot collaborative tasks. Three case studies have been analyzed, including worker counting, motion detection and worker-robot co-presence monitoring.

The protective human-robot separation distance takes into account the worker detection latency, accuracy and robotic motions. Based on these results, the proposed computational approach for data manipulation and feature fusion from heterogeneous IoT sensors is promising for the management of advanced human-robot co-presence situations required in next generation industry processes.

REFERENCES

- [1] P. A. Lasota, T. Fong, and J. A. Shah, "A survey of methods for safe human-robot interaction," *Found. Trends Robot.*, vol. 5, no. 4, pp. 261–349, 2017
- [2] G. Michalos, N. Kousi, P. Karagiannis, et al., "Seamless human robot collaborative assembly – An automotive case study," *Mechatronics*, vol. 55, pp. 194–211, ISSN 0957-4158, <https://doi.org/10.1016/j.2018>.
- [3] F. Vicentini, et al., "Safety Assessment of Collaborative Robotics Through Automated Formal Verification," *IEEE Transactions on Robotics*. doi: 10.1109/TRO.2019.2937471, 2019.
- [4] F. Vicentini, et al., "Trajectory-dependent safe distances in human-robot interaction," in *Proc. IEEE Emerg. Technol. Factory Autom.*, pp. 1–4, Sep. 2014.
- [5] M. Youssef and F. Kawsar, "Transformative Computing and Communication," *Computer*, vol. 52, no. 7, pp. 12–14, July 2019.
- [6] A. Tellaeche, I. Maurtua and A. Ibaruren, "Use of machine vision in collaborative robotics: An industrial case.," *IEEE 21st International Conference on Emerging Technologies and Factory Automation (ETFA)*, Berlin, 2016, pp. 1–6. doi: 10.1109/ETFA.2016.7733689
- [7] J. Lianghai, et al., "Applying Device-to-Device Communication to Enhance IoT Services," in *IEEE Communications Standards Magazine*, vol. 1, no. 2, pp. 85–91, 2017.
- [8] V. Rampa, et al., "Opportunistic sensing in beyond-5G networks: the opportunities of transformative computing," in *The 5G Italy Book 2019: a Multiperspective View of 5G*, pp. 461–475, Edited by CNIT, December, 2019, ISBN 9788832170030.
- [9] Wu et al. "Device-Free WiFi Human Sensing: From Pattern-Based to Model-Based Approaches," *IEEE Comm. Mag.*, vol. 55, no. 10, 2017.
- [10] Savazzi et al., "Device-Free Radio Vision for assisted living: Leveraging wireless channel quality information for human sensing," *IEEE Signal Processing Magazine*, vol. 33, no. 2, 2016.
- [11] Cianca et al., "Radios as Sensors," *IEEE IoT Journal*, vol. 4, no. 2, 2017.
- [12] S. Kianoush, et al., "Passive detection and discrimination of body movements in the sub-THz band: a case study", *Proc of IEEE Conference on Acoustics, Speech and Signal processing (ICASSP)*, 2019.
- [13] S. Savazzi et al., "On the Use of Stray Wireless Signals for Sensing: A Look Beyond 5G for the Next Generation of Industry," *Computer*, vol. 52, no. 7, pp. 25–36, July 2019.
- [14] Wang et al., "Human respiration detection with commodity wifi devices: do user location and body orientation matter" *ACM Ubicomp*, 2016.
- [15] Bartoletti et al., "Device-Free Counting via Wideband Signals," *IEEE J. sel. areas Comm.*, vol. 35, no. 5, 2017.
- [16] S. Savazzi, et al., "Cellular Data Analytics for Detection and Discrimination of Body Movements," *IEEE Access*, vol. 6, pp. 51484–51499, 2018.
- [17] S. Kianoush, et al., "A Cloud-IoT Platform for Passive Radio Sensing: Challenges and Application Case Studies," *IEEE Internet of Things Journal*, vol. 5, no. 5, pp. 3624–3636, Oct. 2018.
- [18] Kong L., et al., "Multi-sensor measurement and data fusion technology for manufacturing process monitoring: a literature review," *International Journal of Extreme Manufacturing*, Vol. 2, 022001, 2020.
- [19] Majumder B.D., et al., "Recent advances in multifunctional sensing technology on a perspective of multi-sensor system: a review," *IEEE Sensors Journal*, vol. 19, no. 4, pp. 1204–1214, Feb. 2019.
- [20] S. Kianoush et al., "Device-Free RF Human Body Fall Detection and Localization in Industrial Workplaces," *IEEE Internet of Things Journal*, vol. 4, no. 2, pp. 351–362, April 2017.
- [21] F. Caccavale, et al., "Bringing Innovative Robotic Technologies from Research Labs to Industrial End-users," Springer, 2020.
- [22] R.-J. Halme, et al., "Review of vision-based safety systems for human-robot collaboration," *Procedia CIRP*, vol. 72, pp. 111–116, 2018.
- [23] M. Linsinger et al., "Situational task change of lightweight robots in hybrid assembly systems," *Procedia CIRP*, vol. 81, pp. 81–86, 2019.
- [24] A. Lismonde, et al., "Trajectory planning of soft link robots with improved intrinsic," *IFAC-PapersOnLine*, vol. 50, no. 1, pp. 6016–6021, 2017.
- [25] "ISO/TS 15066:2016 Robots and robotic devices – Collaborative robots," International Organization for Standardization, Geneva, CH, Standard, 2016.
- [26] F. Vicentini, "Terminology in safety of collaborative robotics," *Robotics and Computer-Integrated Manufacturing*, vol. 63, no. December 2019, p. 101921, 2020.
- [27] A. M. Zanchettin, et al., "Safety in Human-Robot Collaborative Manufacturing Environments: Metrics and Control," *IEEE Transactions on Automation Science and Engineering*, 2016.
- [28] M. Faroni, M. Beschi, and N. Pedrocchi, "An MPC Framework for Online Motion Planning in Human-Robot Collaborative Tasks," *IEEE International Conference on Emerging Technologies and Factory Automation, ETFA*, vol. 2019-Septe, pp. 1555–1558, 2019.
- [29] R. Fornasiero, et al., "Sustainable Networks for WEEE Treatment: A Case Study," *Procedia CIRP*, vol. 41, pp. 276–281, 2016.
- [30] S. Chatterjee and J.S. Simonoff, "Handbook of Regression Analysis," ISBN:9780470887165, 2012,
- [31] N. Pedrocchi, et al., "Safe Human-Robot Cooperation in an Industrial Environment," *International journal on advanced robotic systems*, vol. 10, no. 1, 2013.
- [32] C. Byner, et al., "Dynamic speed and separation monitoring for collaborative robot applications: Concepts and performance," *Robotics and Computer-Integrated Manufacturing*, vol. 58, pp. 239–252, 2019.
- [33] Shur, M. "Subterahertz and terahertz sensing of biological objects and chemical agents", *Proc.SPIE*, 2018.
- [34] Akyildiz, I. F. et al., "Terahertz band: Next frontier for wireless communications," *Physical Communication*, 2014, 12, 16 - 32
- [35] T. Nagatsuma, "Generating millimeter and terahertz waves," in *IEEE Microwave Magazine*, vol. 10, no. 4, pp. 64–74, June 2009.
- [36] S. Scherr, et al., "Miniaturized 122 GHz ISM band FMCW radar with micrometer accuracy," *Proc. of the 2015 European Radar Conference (EuRAD'15)*, pp. 1–4, Paris, France, Sep. 9–11, 2015.
- [37] P. Molchanov, et al., "Short-range FMCW monopulse radar for hand-gesture sensing," *Proc. of IEEE Radar Conference (RadarCon'15)*, pp. 1491–1496, Arlington, USA, May 10–15, 2015.
- [38] Mukherjee, M. et al., "GaN IMPATT diode: a photo-sensitive high power terahertz source *Semiconductor Science and Technology*", 2007, vol. 22, no. 12, pp. 1258, 2007
- [39] V.M. Muravev, et al., "Novel Relativistic Plasma Excitations in a Gated Two-Dimensional Electron System", *Phys. Rev. Lett.* 114, 106805, Published 10 March 2015.
- [40] Ash Tyndall, Rachel Cardell-Oliver, and Adrian Keating, "Occupancy estimation using a low-pixel count thermal imager," *IEEE Sensors Journal*, vol. 16, no. 10, pp. 3784–3791, May 2016.
- [41] S. Savazzi, et al., "Occupancy Pattern Recognition with Infrared Array Sensors: A Bayesian Approach to Multi-body Tracking," *IEEE International Conference on Acoustics, Speech and Signal Processing (ICASSP)*, Brighton, United Kingdom, pp. 4479–4483, 2019.
- [42] S. Palipana and S. Sigg, "Extracting human context through receiver-end beamforming," *IEEE Access*, vol. 7, pp. 154 535–154 545, 2019.
- [43] S. Palipana and S. Sigg, "Receiver-side beamforming to isolate channel perturbations from a human target in a device-free setting," in *The 1st ACM Int. Works. on Device-Free Human Sensing*, 2019.
- [44] S. Palipana and S. Sigg, "Beamsteering for training-free recognition of multiple humans performing distinct activities," *Proc. of IEEE PerCom*, 2020.
- [45] J. Tanaka, et al., "Low power wireless human detector utilizing thermopile infrared array sensor," *Proc. of IEEE Sensors*, pp. 461–465, Valencia, Spain, Nov 2014.
- [46] Yuyi Mao, et al., "A Survey on Mobile Edge Computing: The Communication Perspective," *IEEE Comm. Surveys and Tutorials*, vol. 19, no. 4, 2017.
- [47] L. Mainetti, et al., "A Software Architecture Enabling the Web of Things," *IEEE Internet of Things Journal*, vol. 2, no. 6, pp. 445–454, 2015.
- [48] J.-F. Cardoso and A. Souloumiac, "Blind beamforming for non-gaussian signals," in *Proc. Radar and signal process.*, vol. 140, no. 6. IET, 1993, pp. 362–370.
- [49] E. J. Keogh and M. J. Pazzani, "Derivative dynamic time warping," in *Proc. of the Int. Conf. on Data Mining*. SIAM, 2001.
- [50] N. Sharma et al., "Comparison the various clustering algorithms of weka tools," *Facilities*, vol. 4, no. 7, pp. 78–80, 2012.